Electrophoretic deposition and corrosion performance of Zirconia-Silica composite coating applied on 316L stainless steel and the effect of substrate surface preparation

M. Farhadian[1, 2], K. Raeissi[1], M. A Golozar[1], S. Labbaf[1], T. Hajilou[2], A. Barnoush[2, *]

[1] Department of Materials Engineering, Isfahan University of Technology 84156-83111, Isfahan, Iran

[2] Department of Mechanical and Industrial Engineering, NTNU, Richard Birkelands Vei 2b, 7491 Trondheim, Norway

* Corresponding Author: Afrooz.barnoush (Afrooz.barnoush@ntnu.no)

Abstract

ZrO_2-10 mol.% SiO_2 particles were produced using an alkoxide-based sol–gel method. These were then electrophoretically deposited on surface- treated 316L stainless steel using mechanical polishing, electropolishing, and anodic oxidizing procedures. The coatings were sintered and evaluations confirmed their firm attachment on the oxidized surface, providing an interface including a dense and porous layer. Corrosion studies in a simulated body fluid solution indicated that although the oxidizing treatment had decayed the substrate passivation property, the coating demonstrated the highest barrier effect. A model based on focused ion beam tomography was proposed to describe the interlayer formation on an oxidized substrate.

Keywords: electrophoretic deposition; zirconia; silica; porous surface; corrosion

1. Introduction

The surface treatment of metallic implants to improve the surface biocompatibility and inhibit the release of poisonous ions into the blood has attracted increasing attention [1-4]. Enhancement in the biocompatibility can be achieved by electropolishing the implant substrate or applying biocompatible coatings using different techniques [5-8]. Hydroxyapatite (HA), a bioactive ceramic, has been used to modify the surface of metallic implants; however, its poor mechanical properties such as inherent softness, low hardness, and low fracture toughness limit its application [9]. Zirconia (ZrO_2), a well-known bioceramic, can be applied as a coating to increase the corrosion resistance of metallic implants, especially stainless steel implants, owing to its excellent dimensional and chemical stability, toughness, and Young's modulus similar to stainless steel [10]. Among the three allotropes of ZrO_2, tetragonal, monoclinic, and cubic, the monoclinic phase has indicated greater biocompatibility owing to its ability to form tri-bridged hydroxyl groups (Zr_3-OH), which increases calcium ion adsorption and facilitates apatite nucleation [11]. However, its inability to bond with the bone tissue remains an important restriction for biomedical applications [12]. One approach to increasing the bioactivity of zirconia is the utilization of a suitable component. Silica (SiO_2) as an applicable candidate can not only stabilize the metastable tetragonal phase at low temperatures to prevent aging [13], but also is one of the best components in the bio-glass material group [14]. Further, silanol groups (Si-OH) typically formed on the surface of SiO_2 are assumed to serve as the sites for apatite layer nucleation [15]. It is thought that the silica has a metabolic function that can be effective in cell stimulation towards osteogenesis [16]. Therefore, the combination of the monoclinic phase of ZrO_2 with amorphous SiO_2 is a possible route to overcome the above mention shortcomings of

ZrO_2 and the development of a composite with improved corrosion resistance and the ability to biologically bond to bone tissue for the surface treatment of metallic implants.

Several methods have been reported for applying a ZrO_2-SiO_2 composite coating, such as sol–gel [17] and plasma spray [18]. Although other coating methods such as physical vapor deposition [19] and chemical vapor deposition [20] can be applied for ceramics, they are costly and not suitable for mass production. In the plasma spray technique, the chemical composition cannot be controlled precisely owing to the high temperature during the coating process. Further, zirconium-silicone compounds such as Zr_5Si_4 and Zr_2Si phases are formed from molten particles owing to the interdiffusion of Si and Zr atoms at the interface of the ZrO_2 and SiO_2, which degrades the chemical properties of the composite material [18]. These new phases can also negatively influence the mechanical properties and biological response of the composite. Sol–gel-based coatings cannot provide an effective protective layer owing to the difficulty of producing a coating with uniform thickness and the tendency to form cracks under drying, which deteriorates the barrier property [21]. Electrophoretic deposition (EPD) is a low-cost and attractive method to produce ceramic coatings with the ability to control the thickness and chemical composition [22]. Preparing a highly stabilized colloidal suspension is a prerequisite for producing a high-quality coating through this method. However, the major limitation of EPD is the low adhesion of the coating to the substrate. Several methods have been studied to increase the coating adhesion, such as sintering, adding polymer binders to the coating, and using smaller-sized particles in the suspension [23].

Previous studies have applied composite oxide coatings containing ZrO_2 and SiO_2 particles to improve the corrosion resistance, mechanical properties, and surface bioactivity [18, 24, 25]. For example, Srinivasan et al. [26] prepared ZrO_2/SiO_2 coatings produced by sol–gel on 316L

stainless steel and a significant improvement in corrosion resistance along with HA growth was reported for Si:Zr, atomic ratio of 50:50. Further, an enhancement of bioactivity by adding calcium phosphate to ZrO_2 coatings has been reported [27]. According to Mork et al. [28], HA with 10–20 wt.% SiO_2 can significantly improve the bonding strength of HA/SiO_2 plasma sprayed coatings on stainless steel substrate. A composite bilayer coating of yttria-stabilized zirconia (YSZ)/bioactive bio-glass (45S5) on Ti6Al4V substrate has been reported [29] to produce a coating with enhanced mechanical strength and promoted surface bioactivity properties.

In the present work, a ZrO_2-SiO_2 coating is produced using the EPD process of composite particles on 316L stainless steel that was surface treated using different electrochemical treatments to improve the adhesion strength and corrosion performance. Important parameters related to the suspension and process are optimized to achieve high quality coatings. The corrosion resistance of the obtained coatings is investigated in a simulated body fluid (SBF) solution and compared with bare surface-treated substrates.

2. Experimental

2.1 Preparation of ZrO_2-10 mol.% SiO_2 composite particles

In this study, the alkoxide-based sol–gel method was used to prepare the ZrO_2-10 mol.% SiO_2 (Z10S) composite particles in a manner similar to the procedure described in ref. [13]. Zirconium propoxide (70 wt.% in propanol from Sigma Aldrich) and tetraethyorthosilicate (TEOS) (Sigma Aldrich) were used as precursors. To synthesis the particles, two separate solutions were prepared. For the first solution, 50 ml of zirconium propoxide was dissolved in 20 ml of 2-methoxyethanol (Sigma Aldrich) as a chelating agent. Then, 2.3 ml of TEOS solution was added.

In the second solution, 4 ml deionized water at pH 11 (pH was adjusted by ammonia solution) as a catalyst agent was diluted by 40 ml of 2-methoxyethanol. It should be mentioned that the hydrolysis rate of zirconium propoxide is different from that of TEOS and it must be chelated to prevent phase separation during the hydrolysis step. Thereafter, both prepared solutions were mixed and stirred approximately 30 min until gelation occurred. The gels were dried at room temperature and mixed with an EtOH/OH solution (95/5 vol.%) at 60 °C in a water bath at four intervals of 24 h to extract the organic phase. The obtained gel was dried at 100 °C and then heat-treated at 1100 ºC for 4 h to obtain a monoclinic phase structure.

2.2 Suspension preparation and electrophoretic deposition

Owing to formation of hard agglomerates during the heat treatment of the gel, the particles were ball milled in a placatory machine using a zirconia jar and balls with a weight ratio of 20:1, balls to powder, for up to 2 h. Then, they were wet-ball milled for 24 h in ethanol containing 3 wt.% polyethylenemine (PEI) (Sigma Aldrich, MW = 10000) as a surfactant using a polymeric cup and zirconia balls. Then, a suspension with particle dosage of 5 g l^{-1} was prepared in EtOH (as the solvent). Iodine with different concentrations including 0.1, 0.2, 0.3, 0.4, and 0.5 g l^{-1} was added to the solution and the changes in pH, conductivity, zeta potential, and particle size distribution were recorded.

Stainless steel 316L in a disc shape, 14 mm diameter and 3 mm thickness, served as both the working and counter electrodes. The chemical composition of the 316L (wt.%) was as follows: Cr: 16.6, Ni: 13.1, Mn: 1.73, Mo: 1.97, Si: 0.2, C: 0.024, and Fe: remainder. The distance between the two electrodes was adjusted to 2 cm in all experiments. The surface of the working electrodes was mechanically polished by SiC papers up to 1200 grit and then rinsed in water, ethanol, and acetone for 10 min for cleaning the surface (called the S1 substrate). The porous

surface was achieved on the same prepared substrate by anodic oxidizing at 12 V for 6 min in a solution containing 60 wt.% sulfuric acid (98 wt.% from Merck), 20 wt.% H_3PO_4 (98 wt. % from Merck), 10 wt.% glycerol (Merck), and 10 wt.% deionized water (called the S2 substrate). Electrochemical surface polishing was conducted [30]. Before the electropolishing, the substrate was mechanically polished up to 4000 grit with SiC papers, followed by polishing with 1 μm diamond paste, and finally electropolished at 4 V for 3 min in the above-mentioned solution (called the S3 substrate).

The electrophoretic deposition process was conducted using a DC power supply at a constant voltage regime. To produce high quality coatings, an optimization of the most important parameters related to the suspension and EPD process was performed. The coatings were dried at 400 ˚C for 2 h, and then sintered at 1100 ˚C for 2 h in vacuum (10^{-5} torr) with heating and cooling rates of 2 ˚C/min to obtain a high compact coating.

2.3 Characterizations

The zeta potential and size distribution of the particles were measured using a zeta sizer (Beckman counter Delsanano). Phase analysis was performed by X-ray diffraction (XRD, Philips X'pert) at a scanning rate of 3°/min with a step size of 0.02° in the 2θ range from 20° to 80°. Fourier-transform infrared (FTIR, Jasco-680) spectroscopy was used to determine the functional groups and chemical bondings of the coatings in the range of 400 to 4000 cm^{-1}. The amounts of PEI adsorbed to the particles were measured by a thermogravimetric and differential thermal analysis (TGA and DTA, respectively). The surface morphology, thickness values (from cross-sectional views), and chemical composition of the coatings were studied by a scanning electron microscope (SEM, FEI Helios) equipped with an energy dispersive spectroscopy (EDS). An

infinite focused microscope (IFM, Alicona) was applied to study the surface topography and surface roughness of the coatings. To evaluate the electrochemical behavior of the coatings, potentiodynamic polarization tests and electrochemical impedance spectroscopy (EIS) were performed using a potentiostat/galvanostat (Gamry). All tests were performed at similar conditions in an SBF at 37 °C after immersion for 24 h to establish the open circuit potential (OCP) prior to running each test. All measurements were performed in a typical three-electrode cell where a saturated calomel electrode served as the reference electrode, a platinum plate was applied as the counter electrode, and uncoated/coated specimens were used as the working electrode. Polarization tests were conducted over a potential ranging from -500 to 1500 mV with respect to the OCP using a scan rate of 1 mV/s. EIS tests were performed under the same setup and conditions described previously for the polarization tests using a potential amplitude of 10 mV over a frequency range from 100 kHz to 10 mHz. The EIS data were processed and fitted using Zview software and the electrical equivalent circuit (EC) model. Focused Ion Beam (FIB) with a dual beam system (FEI) was applied to study the interface structure using the slice and view method.

3. Results and discussion

3.1 Characterization of suspension solution

Fig. 1 displays the SEM observation of Z10S composite particles after 0, 0.5, 1, and 2 h ball milling. Clearly, the heat-treated particles (Fig. 1a) indicate a dense aggregated structure consisting of smaller parts up to 14 µm. The presence of such large particles in the suspension results in the instability of the suspension, which leads to the formation of coatings with low cohesion strength, high porosity, and unacceptable sintering behavior [31]. Hence, decreasing the

particle dimensions to submicron size using a ball mill is mandatory [32]. By increasing the ball-milling time, the particle size reduced, achieving approximately 300 nm after 2 h (Fig. 1d). However, a further increase of the milling time resulted in the reattachment and formation of agglomerated particles. Thus, the submicron particles obtained after 2 h ball milling were used to prepare a stable suspension for the EPD process.

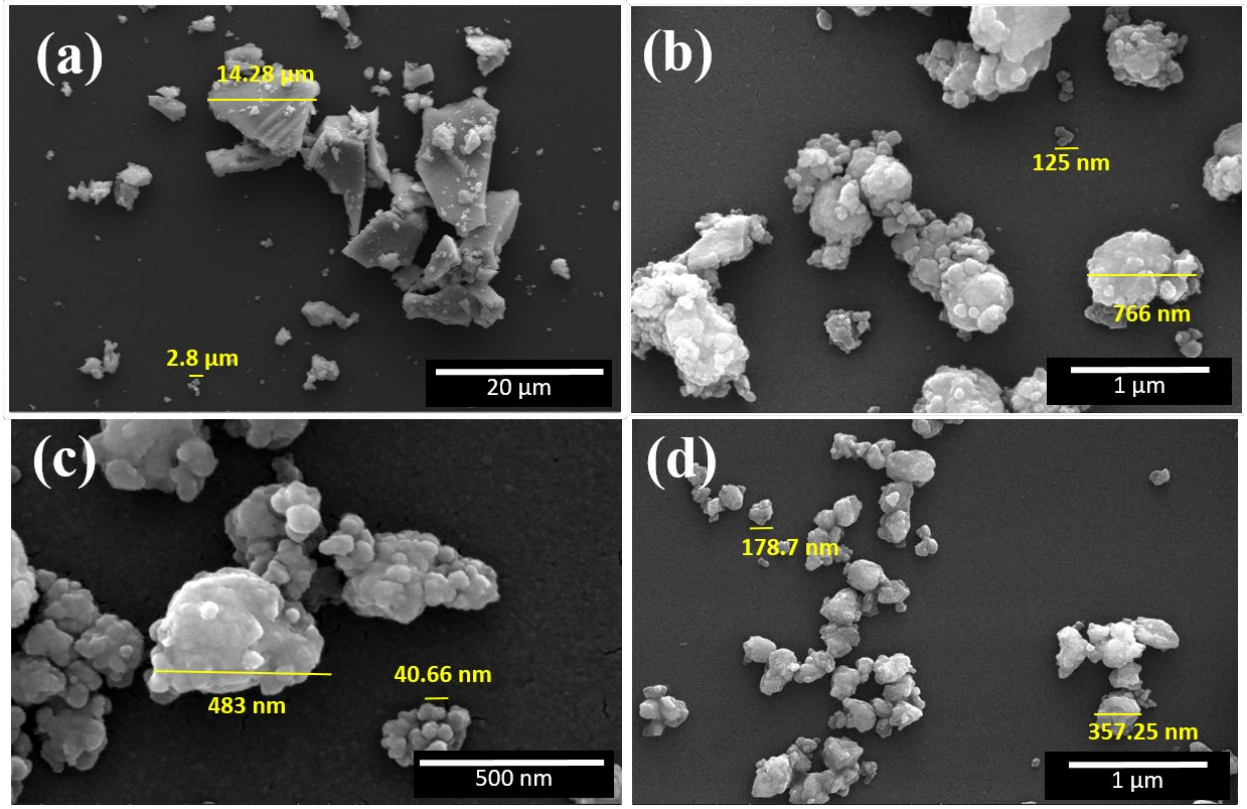

Fig. 1. SEM images from Z10S particles after: (a) heat-treated at 1100 °C for 4 h and ball-milled after: (b) 0.5, (c) 1, and (d) 2 h.

The achievement of a stable suspension containing particles with minimum agglomeration is a prerequisite requirement for producing a coating with minimum defects. Moreover, particle size distribution strongly influences the suspension stability necessary for obtaining a high quality coating in the EPD process [33]. There is no general rule in this case; however, according to the literature, the average particle size should not be greater than 30 µm, otherwise they have a

strong tendency to settle owing to gravity [34]. Conversely, very fine particles have a tendency to agglomerate to decrease their surface energy. The driving force for sintering is also the reduction of excess surface energy, which is greater for finer particles; hence, they sinter more easily [35]. However, using submicron particles in the EPD process results in high density and low porosity coatings if the particle size is maintained at its primary dimension to prevent agglomeration during deposition [36]. For this purpose, the agglomeration can be controlled by the adsorption of a suitable surfactant on the surface of the particles. PEI is a cationic surfactant that can effectively decrease the agglomeration by electro-steric forces where the charged aliphatic chains of the polymer attached to the particle surface act as a barrier to prevent agglomeration. In this manner, a combination of electrostatic repulsion, steric repulsion, and van-der-Waals attraction result in electro-steric stabilization [37]. Moreover, the amine groups in the PEI can be charged by the adsorption of a proton from the suspension media [38], which further assists the stabilization. The amount of PEI added to the suspension was 3 wt.% relative to the Z10S powders.

To study the efficiency of PEI adsorption on the surface of the particles, TGA-DTA and FTIR analysis were conducted; their results are presented in Fig. 2. According to the thermal analysis results, the adsorption efficiency of PEI is approximately 2.2 wt.%, implying that the remainder of the PEI (i.e., approximately 0.8 wt.%) has left the suspension, which leads to an increase in the suspension conductivity [39]. The exothermic peak near 300 °C (Fig. 2a) indicates the burning of PEI from the composite structure.

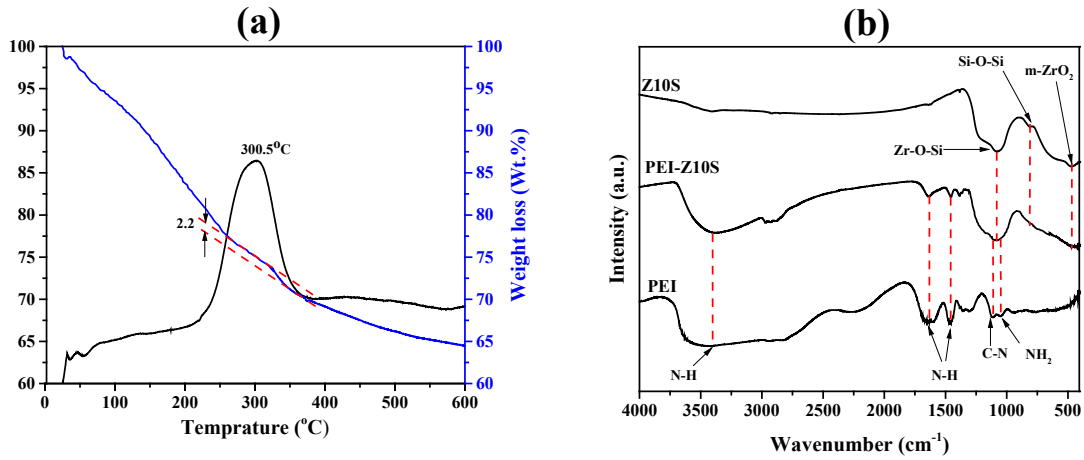

Fig. 2. (a) TGA-DTA from PEI-Z10S particles and (b) FTIR analysis of PEI, PEI-Z10S, and Z10S particles.

Fig. 2b displays the FTIR spectra of the PEI, Z10S, and PEI-modified Z10S particles. As can be observed from the FTIR spectrum of the Z10S, the peak at 480 cm^{-1} is attributed to the vibration of the Zr-O bonds in the monoclinic structure of the ZrO_2. Characteristic peaks of monoclinic ZrO_2 were reported in the frequency range from 345 to 732 cm^{-1} and overlapped with the vibration of the non-bridging Si-O^- groups near 600 cm^{-1} [40, 41]. The peak appearing at 800 cm^{-1} can be ascribed to the stretching vibration of the Si-O-Si bonds. The peak at 1070 cm^{-1} is caused by the bending vibration mode of the Zr-O-Si formed during the condensation reaction overlapped with the sharp and broad peak of the Si-O-Si bonds, which makes it difficult to distinguish. The peaks at 1630 and 3400 cm^{-1} correspond to the bending and stretching vibration of the O-H functional group, respectively [42]. For the PEI, the peaks appearing at 3500 and 1500 cm^{-1} are related to the stretching and bending vibrations of the N-H in the PEI structure, respectively. The peaks appearing at 1000 and 1100 cm^{-1} correspond to the NH_2 functional groups and N-H bonds, respectively [39, 43]. According to the FTIR spectra, the peaks related to PEI are also present in the PEI-Z10S sample, proving that the PEI is adsorbed on the surface of the particles. This can confirm that the PEI adsorption mechanism is dominated by electrostatic

interactions as well as the formation of hydrogen bonding between the amine functional groups from the PEI molecules and the hydroxyl groups on the surface of the particles [39].

The proton concentration in the EtOH solvent is not sufficient for charging the surface of the PEI-modified particles. Thus, in an effort to supply additional protons, iodine was added to the EtOH (see Eq. 1). In this manner, protons could be adsorbed by the amine groups (Eq. 2) and the I^- anions repelled from the surface, leading to the formation of a double layer [44].

$$CH_3 - CH_2 - OH + I_2 \rightarrow ICH_2 - CH_2 - OH + I^- + H^+ \quad (1)$$

$$(ZrO_2/SiO_2) - NH_2 + H^+ \rightarrow (ZrO_2/SiO_2) - NH_3^+ \quad (2)$$

Thus, the particles were positively charged, which follows the cathodic EPD process under the applied voltage. The effect of the iodine concentration on the size distribution of the Z10S particles is displayed in Fig. 3 and the average particle size values are listed in Table 1. As can be observed, the average particles size of Z10S in pure EtOH is approximately 1.2 µm; whereas it decreases to approximately 0.35 µm in a 0.3 g l^{-1} iodine concentration. However, adding more iodine to the suspension results in an increase of the average particle size to 0.54 µm.

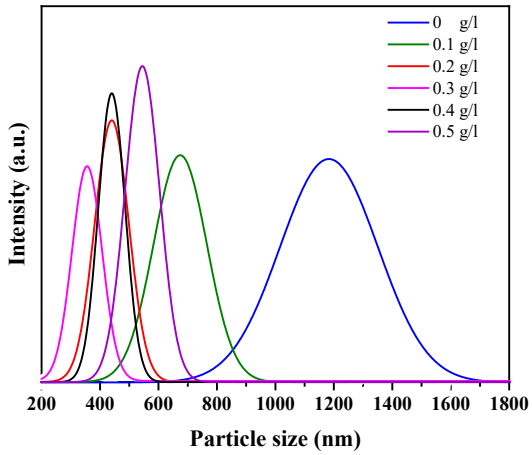

Fig. 3. Size distribution of Z10S particles as a function of iodine concentration in EtOH solvent.

Table 1. Average particle size of nanocomposite powder dispersed in EtOH solvent containing different iodine concentrations

Iodine concentration (g l^{-1})	Average particle size of Z10S powder (µm)
0	1.2
0.1	0.68
0.2	0.46
0.3	0.35
0.4	0.44
0.5	0.54

The mass deposited by the EPD process is a function of the parameters related to the suspension and process. At the initial time of deposition, the deposited mass per unit area follows Eq. 3.

$$w = \frac{2}{3} C\varepsilon_0 \varepsilon_r \xi \eta^{-1} E L^{-1} t \quad (3)$$

where C is the particle concentration in the suspension, ε_0 is the vacuum permittivity, ε_r is the relative solvent permittivity, ξ is the zeta potential, η is the viscosity, E is the applied voltage, L is the distance between the electrodes, and t is the deposition time. In the present work, the effect of the zeta potential, deposition time, and applied voltage on the coating quality were studied. According to Eq. 3, the zeta potential is one of the most important parameters in the EPD process; this can be influenced by the type of solvent, and type and concentration of the charging agent [22]. Fig. 4 displays the changes in pH, conductivity, zeta potential, and deposited mass as a function of the iodine concentration in the suspension. The ideal suspension for the EPD process should have low ionic conductivity and a high zeta potential value. At high iodine concentration, the ionic conductivity is increased and the number of protons moving toward the substrate under applied voltage is increased, leading to a reduced cathodic current efficiency. Moreover, high values of conductivity reduce the double layer thickness, resulting in decreasing electrophoretic mobility [22]. According to the obtained values for zeta potential, deposited

weight mass, and particle size distribution, 0.3 g l^{-1} of iodine was chosen as the optimum concentration.

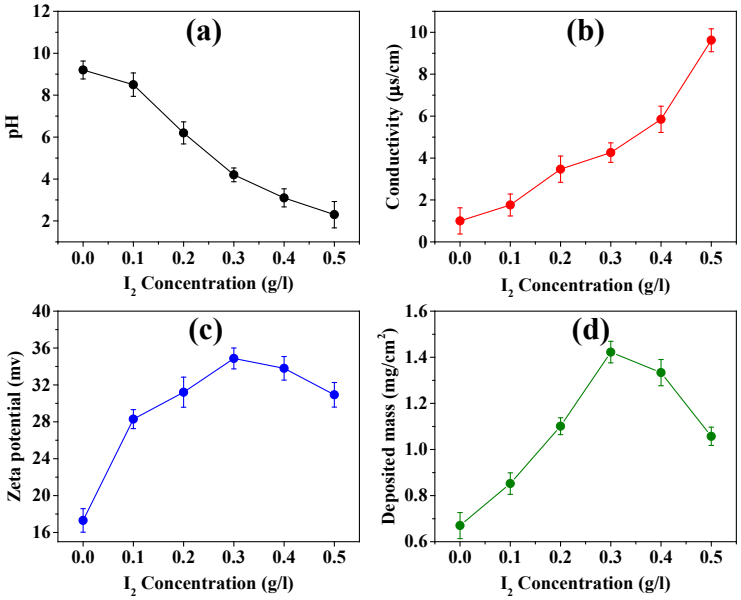

Fig. 4. Effect of iodine concentration on: (a) pH, (b) conductivity, (c) zeta potential, and (d) deposited mass of Z10S suspension.

Fig. 5 displays the effect of pH on the surface topography of the Z10S coating deposited on the mechanically polished substrate (S_1 substrate) at 15 V. The pH was adjusted to 8, 6, 4, and 2 by adding iodine to the suspension. Clearly, the surface of the coating obtained in 0.1 g l^{-1} iodine (i.e., pH 8) (Fig. 5d) is uneven because of the low electrophoretic mobility. In this condition, the relative zeta potential is low (Fig. 4c) because the particles' surface cannot be effectively charged, making the suspension unstable. Consequently, the particles tend to agglomerate and settle owing to gravity. At pH 2, increasing the ionic strength by adding additional iodine causes the double layer to be thinner, decreasing the zeta potential (Fig. 4c). Therefore, the particles combine while drifting toward the substrate and produce a coating consisting of aggregated particles with a non-uniform surface (Fig. 5a). Moreover, increasing the ionic conductivity

disturbs the movement of the particles owing to the migration of the ions. At pH 4 (0.3 g l^{-1} iodine), the particles reveal the highest zeta potential providing acceptable suspension stability, which produces a coating with the smoothest and most homogeneous surface, as displayed in Fig. 5b.

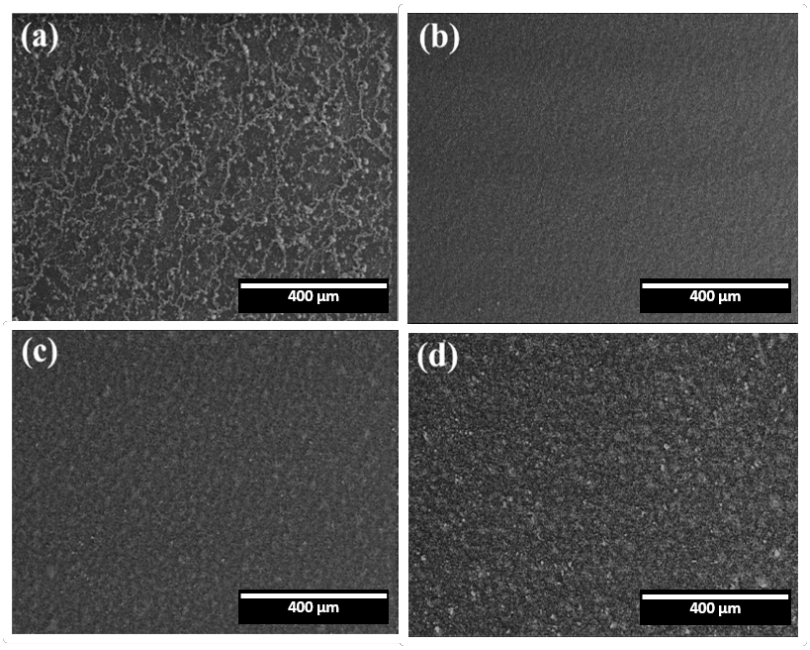

Fig. 5. SEM observation of surface morphologies of Z10S coating deposited on S1 substrate at 15 V and pH: (a) 2, (b) 4, (c) 6, and (d) 8.

3.2 Substrate surface treatment

Fig. 6 illustrates the infinite focused microcopy (IFM) images captured from 316L stainless steel substrate treated by different surface preparation methods. In brief, three different procedures were applied to prepare the substrate surface before the EPD process, including mechanical polishing using SiC papers up to 1200 grit (S_1 substrate, Fig. 6a), anodic oxidation resulting in a porous surface (S_2 substrate, Fig. 6b), and electrochemical polishing, which provides a smooth atomically-clean surface (S_3 substrate, Fig. 6c). The roughness parameter values of the S_1, S_2, and S_3 substrates are listed in Table 2. As reported previously [30], anodic oxidation could improve the corrosion resistance and biocompatibility of the 316 stainless steel substrate. It was

found that the thickness and atomic Cr/Fe ratio of the oxide layer formed after anodic oxidation were greater than that of the natural oxide film [30]. Therefore, both the roughness and surface chemical composition of the 316L were modified by the anodic oxidation treatment.

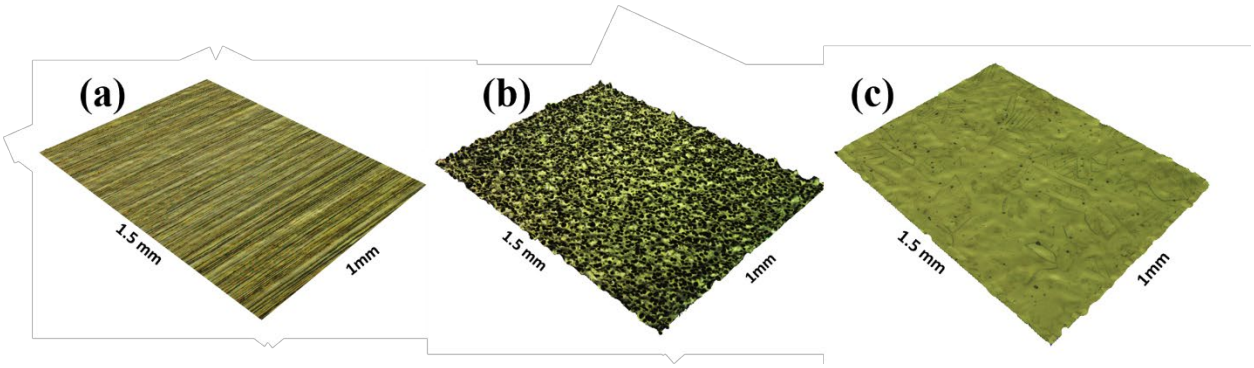

Fig. 6. IFM 3D images from 316L substrate treated by different procedures: (a) S1, (b) S_2, and (c) S_3.

Table 2. Roughness parameter values of substrate treated with different surface preparation methods

Roughness parameters	Sample code		
	S_1	S_2	S_3
Ra (nm)	54	1459	26
Rz (nm)	435	9317	9317
Rq (nm)	68	1857	36

3.3 Optimizing electrophoretic deposition parameters

Fig. 7 displays the effect of the applied voltage on the surface morphology of the coatings deposited from the suspension at pH 4 on S_1 substrate at different potentials. At 10 V, the substrate is not completely covered (Fig. 7b), which means that there is not sufficient electrophoretic mobility to move the positively charged particles toward the cathode. By increasing the voltage to 15 V, a coating with a uniform surface is achieved owing to the acceptable arrangement of fine particles (Fig. 7b). By further increasing the voltage to 20 and 25 V, according to the inset images in Figs. 7c and d, the agglomerated particles beside the fine

particles result in a non-uniform surface. In these cases, the velocity of the particles has been enhanced by increasing the applied voltage, which prevents the deposition of particles at the appropriate sites and results in coatings with non-uniform surfaces. In addition, the high voltage can cause turbulence in the suspension [22], which removes the particles loosely attached on the surface and causes a wavy-shaped topography. Hence, 15 V was found to be the optimum voltage to provide sufficient electrophoretic mobility, leading to a coating with a smooth surface. Thus, this voltage was considered for further investigations.

To achieve a thick coating with low defects and acceptable barrier properties in the EPD process, investigating the effect of deposition time was also required. At low thickness, the coating demonstrates no barrier effect against corrosive media. Conversely, a coating with high thickness indicates numerous cracks after sintering, which provides easy routes for inward diffusion of corrosive species. Coating thickness and deposited mass per unit area as a function of deposition time are illustrated in Fig. 8. As can be observed, the coating thickness linearly increases with time and tends to achieve a plateau at approximately 50 μm after 60 min. According to the Hamaker equation [45], the mass of the deposits in the EPD process should linearly increase with increasing time; however, after a long deposition time, the mass deviates from linearity and achieves a plateau [46]. At the long deposition time, the effective applied voltage between the electrodes decreased owing to the growth of a non-conductive layer on the substrate resulting in a decrease of particle mobility.

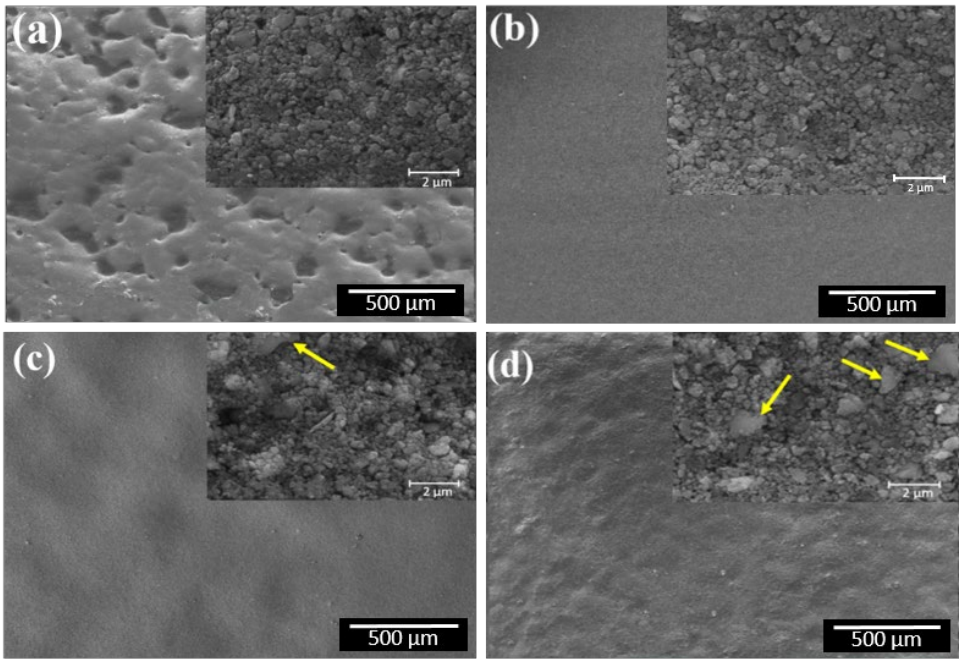

Fig. 7. SEM of surface morphologies of Z10S coating deposited on S1 substrate at: (a) 10, (b) 15, (c) 20, and (d) 25 V.

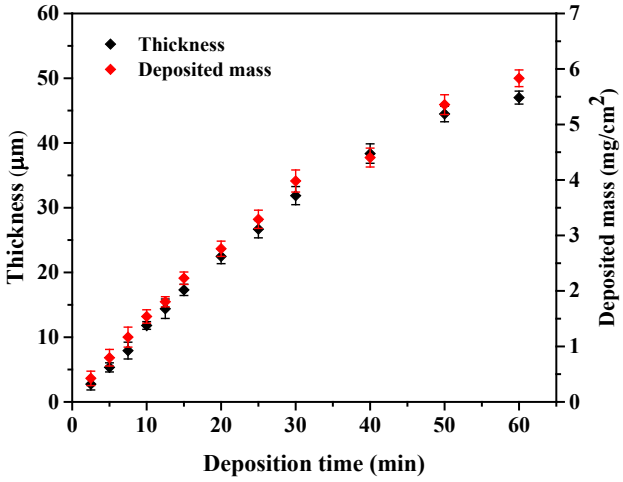

Fig. 8. Coating thickness and deposited mass of Z10S particles as a function of deposition time.

Fig. 9 displays IFM images of C_1 (Z10S coating on S_1), C_2 (Z10S coating on S_2), and C_3 (Z10S coating on S_3) samples after sintering at 1100 °C for 2 h. The roughness parameters were measured using optical profilometry and are listed in Table 3. According to the obtained results,

the C_2 and C_3 coatings demonstrated the highest and the lowest Ra values, respectively, which corresponds to the roughness of the substrate surface (Table 2). It is worth mentioning that the substrate roughness strongly influenced the topography of the resulting coatings.

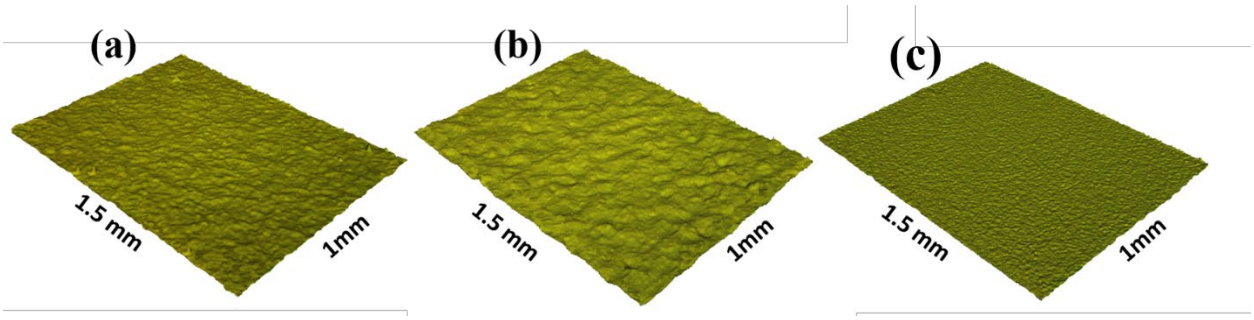

Fig. 9. IFM images from Z10S coatings: (a) C1, (b) C_2, (c) C_3.

Table. 3. Roughness parameters of Z10S coatings produced on different surface-treated substrates

Roughness parameters	Sample code		
	C_1	C_2	C_3
Ra (nm)	291.12	467.93	103.26
Rz (nm)	1491.20	2430.00	489.83
Rq (nm)	364.31	612.73	131.98

Variation of current density as a function of deposition time when 15 V was applied is illustrated in Fig. 10 for the different surface-treated substrates. The wet deposits on the substrate can be considered as Z10S particles with high resistance along with the pores filled with electrolyte. Thus, the current can be established through the pores during the coating growth on the substrate. Therefore, the resistance of the wet deposits is determined by the solution trapped between the particles and consequently is closely related to the coating porosity. Therefore, the greater the coating porosity, the greater the current density. The decrease of current density during the EPD process is due to the increase of the coating thickness, which reduces the porosity. Clearly, the

C_2 sample demonstrated the lowest current density in comparison with C_1 and C_3 (Fig. 10). It can be concluded that the C_2 sample can be considered as the most compact coating.

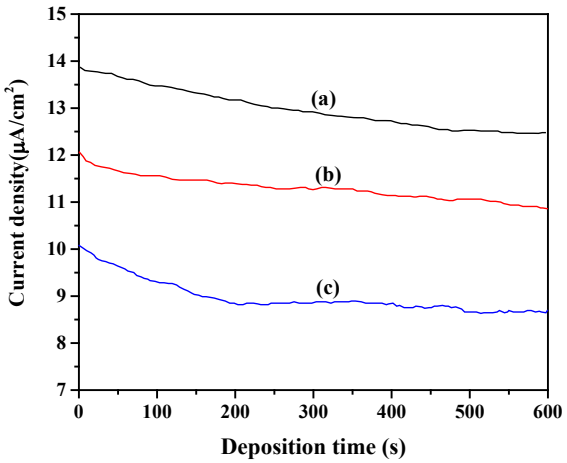

Fig. 10. Current density measured during the EPD process of Z10S particles on: (a) S_1, (b) S_2, and (c) S_3 substrates.

There are three general strategies for the adhesion of ceramics to metal surfaces. The first is mechanical adhesion achieved through building up a mechanical interlocking between the components and substrate. The second is direct attachment, where the components bond to the substrate either through a solid-state process or fusion. The third is indirect; an intermediate layer creates the bond between the coating and substrate [47]. However, coating adhesion through the EPD process is mainly through mechanical interlocking. Fig. 11 represents the SEM cross-sectional views of C_1, C_2, and C_3 coatings indicating the same thickness, approximately 20 ± 1 μm. Clearly, the C_3 coating produced on the electropolished substrate with a smooth surface demonstrates a mechanical interaction without apparent interlocking at the interface. By increasing the roughness of the substrate by mechanical polishing, mechanical interlocking is promoted (C_1 coating). Conversely, for the C_2 coating, it appears that the particles are located

inside the substrate porosities (oxide pores) creating an effective mechanical interlock at the interface (Fig. 11b). This results in greater adhesion strength.

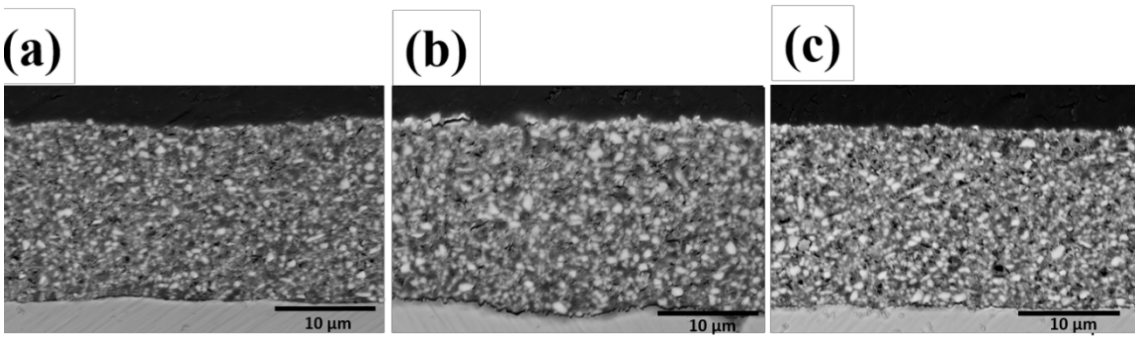

Fig. 11. Cross-sectional view of Z10S coating of: (a) C_1, (b) C_2, and (c) C_3 samples.

To study the effect of the substrate surface treatment on the sintering behavior of the resulting coatings, the coatings were sintered at 1100 and 1200 °C for 2 h in a vacuum. SEM images from the coatings surface are displayed in Fig. 12. The coatings sintered at 1100 °C indicate acceptable sintering behavior; that is, crack-free surfaces with no delamination. As can be observed, the topography of the sintered coatings is influenced strongly by the surface roughness of the substrate, where the roughness of the coatings decreases as $C_2 > C_1 > C_3$. By increasing the sintering temperature to 1200 °C, numerous cracks and peeling are observed, especially for the C_1 and C_3 samples. As indicated in Figs. 12d and f, the C_1 and C_3 coatings become wrinkled, indicating that there was insufficient adhesion between the substrate and coatings. However, the coating applied on the S_2 substrate (i.e., C_2 coating) indicates small defects along with a minor change in surface topography (Fig. 12e), demonstrating that the surface roughness of the substrate has a key role during the sintering process. This could be related to the strong mechanical interlocking present at the coating/substrate interface before sintering. A mismatch between the coefficient of thermal expansion (CTE) for the 316L substrate and ceramic coating

components results in delamination at high temperature because it causes strong thermal stress, especially at the interface. The thermal stress influences the coating quality by forming cracks, residual stress, and bonding strength loss. The CTE of 316L, ZrO_2, and SiO_2 are reported to be 19.1×10^{-6}, 10.6×10^{-6}, and 0.75×10^{-6} K^{-1}, respectively [48]. Because the CTE of the coating is less than that of the substrate, contraction occurring on cooling in the coating would be less than that of substrate. In this case, the strong mechanical interlocking existing before sintering at the coating/substrate interface of C_2 sample can successfully prevent adhesion loss. Typically, the major concerns in the development of biocompatible ceramic coatings are low bonding interface strength and low cohesion strength of the coating, being limited by factors such as non-uniform coating thickness, delamination due to thermal stress, and weak interface bonding [49].

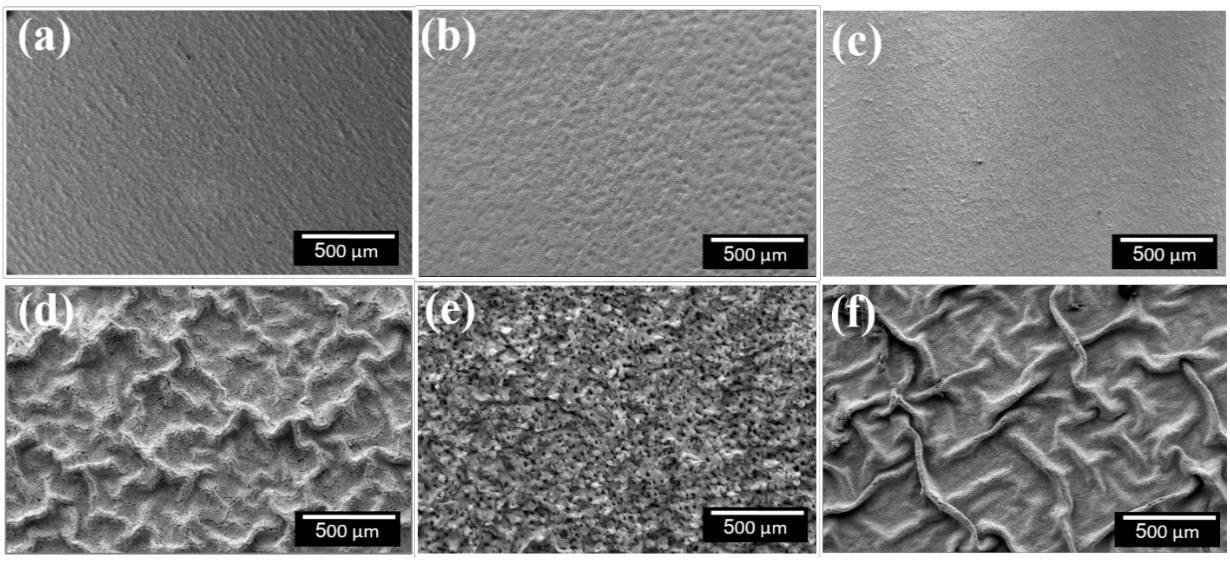

Fig. 12. SEM images of sintered Z10S coatings of: (a) C_1, (b) C_2, and (c) C_3 samples at 1100 °C and (d) C_1, (e) C_2, and (f) C_3 samples at 1200 °C with heating rate of 2 °C/min for 2 h in vacuum furnace under pressure of 10^{-5} torr.

3.4 Phase and chemical compositions of the coating

The phase and chemical compositions of Z10S coating applied on 316L substrate after sintering at 1100 °C for 2 h were investigated using XRD and EDS analysis, respectively (Fig. 13). As indicated in Fig. 13a, all the diffraction peaks appearing in the XRD pattern relate to the monoclinic structure of ZrO_2, which in turn confirms that no traces of other ZrO_2 allotropic phases (such as tetragonal or cubic) or crystalline SiO_2 phases exist in the coating. It should be noticed that the diffraction peaks related to the crystalline structure of SiO_2 (quartz) cannot be observed in ZrO_2-SiO_2 binary oxide systems at the temperatures up to 1200 °C [50]. Fig. 13b displays the EDS spectrum from the surface of the Z10S coating indicating that the Zr/Si ratio of the coating is 10.8, which is similar to the early nominal composition of the ZrO_2-10 mol.% SiO_2 particles synthesized by the sol–gel method. Considering the XRD, EDS, and FTIR (Fig. 2b) results, it can be concluded that the composite coating consists of monoclinic ZrO_2 and amorphous SiO_2 with no trace of impurities. Similar ZrO_2-SiO_2 composite coatings have been prepared using a plasma spray technique [18]. According to the results of this study, a heterogeneous chemical composition across the coating was achieved owing to the presence of unmelted silica particles with circled or irregular shapes and zirconium silicide impurities [18].

Further information can be obtained by studying the interface after sintering using FIB-cross-sectional observation (Fig. 14). For the C_1 and C_3 coatings, the particles near the interface appear to be attached to the substrate through mechanical interlocking only, without forming an interlayer (Figs. 14a and e). Conversely, a dense interlayer of approximately 1.3 μm thickness is formed at the coating/substrate interface in the C_2 coating (Fig. 14c). Fig. 14d indicates that this interlayer is rich in Cr and Mn elements. The anodic oxidation treatment of the 316L stainless steel is responsible for increasing the Cr and Mn content of the surface. Based on the literature

[30], the major component of an anodic oxide layer is chromium hydroxide, which converts to chromium oxide through sintering; this could create a dense intermediate layer with simultaneous integration of the ZrO_2-10 mol.% SiO_2 particles embedded earlier in the porosity of this oxide layer. This results in a stronger interface adhesion by enhancing the chemical (covalent) bonding. Therefore, in addition to increasing the surface roughness, the produced anodic oxide layer can effectively increase the adhesion strength of the coatings after sintering. Similar results indicate that a porous alumina layer produced by anodic oxidation on an Al surface enhanced the adhesion of SiO_2 and TiO_2 nanoparticles through the EPD process [51] and that a TiO_2 interlayer improved the adhesion strength of HA coating on a Ti substrate [52]. Fig. 15 displays the EDS maps of the samples obtained from the defined rectangular regions at the interface of the SEM-FIB cross sections in Fig. 14. As can be observed in Fig. 15a, no sign of elemental diffusion or enrichment can be detected at the coating/substrate interface of the C_1 sample. For the C_3 sample, there is also a limited enrichment of the Cr and Mn elements at the interface as indicated in Fig. 15c. However, the EDS maps in Fig. 15b clearly indicate the enrichment of Cr and Mn at the interface of the C_2 sample indicating the formation of an oxide interlayer during the sintering process.

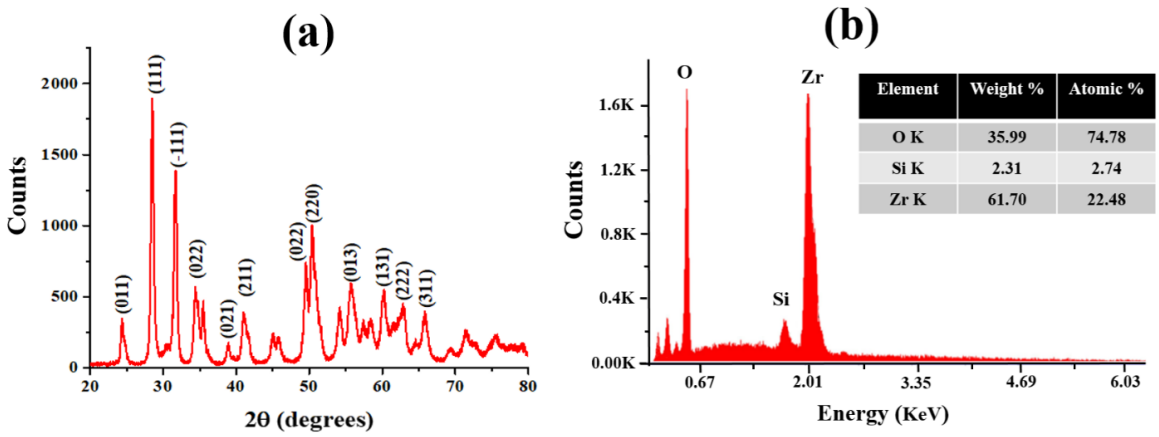

Fig. 13. (a) XRD pattern and (b) EDS spectrum from the surface of Z10S coating.

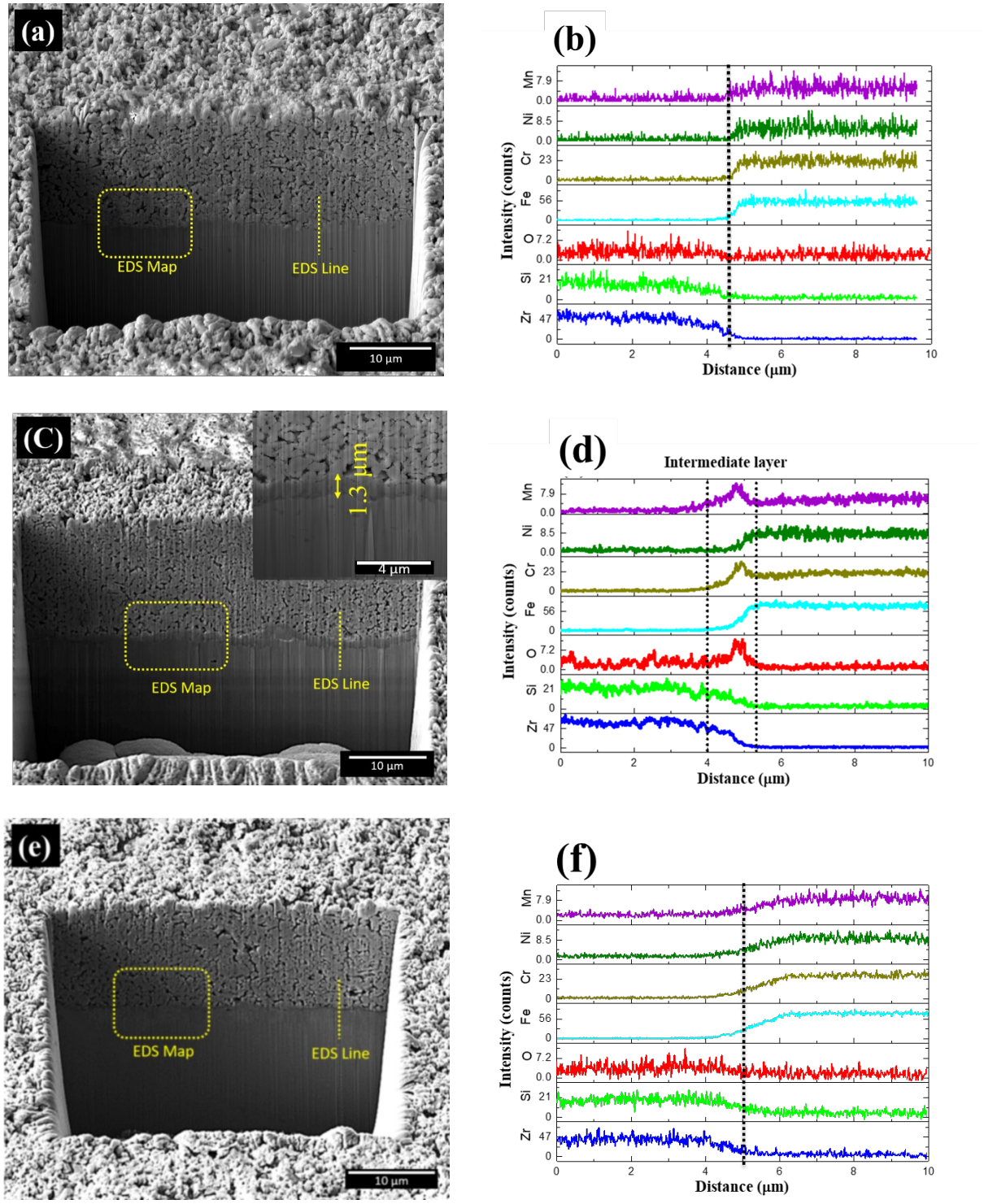

Fig. 14. FIB cross-sectional views of: (a) C_1, (c) C_2, and (e) C_3 and line EDS spectrums of (b) C_1, (d) C_2, and (f) C_3 coating samples.

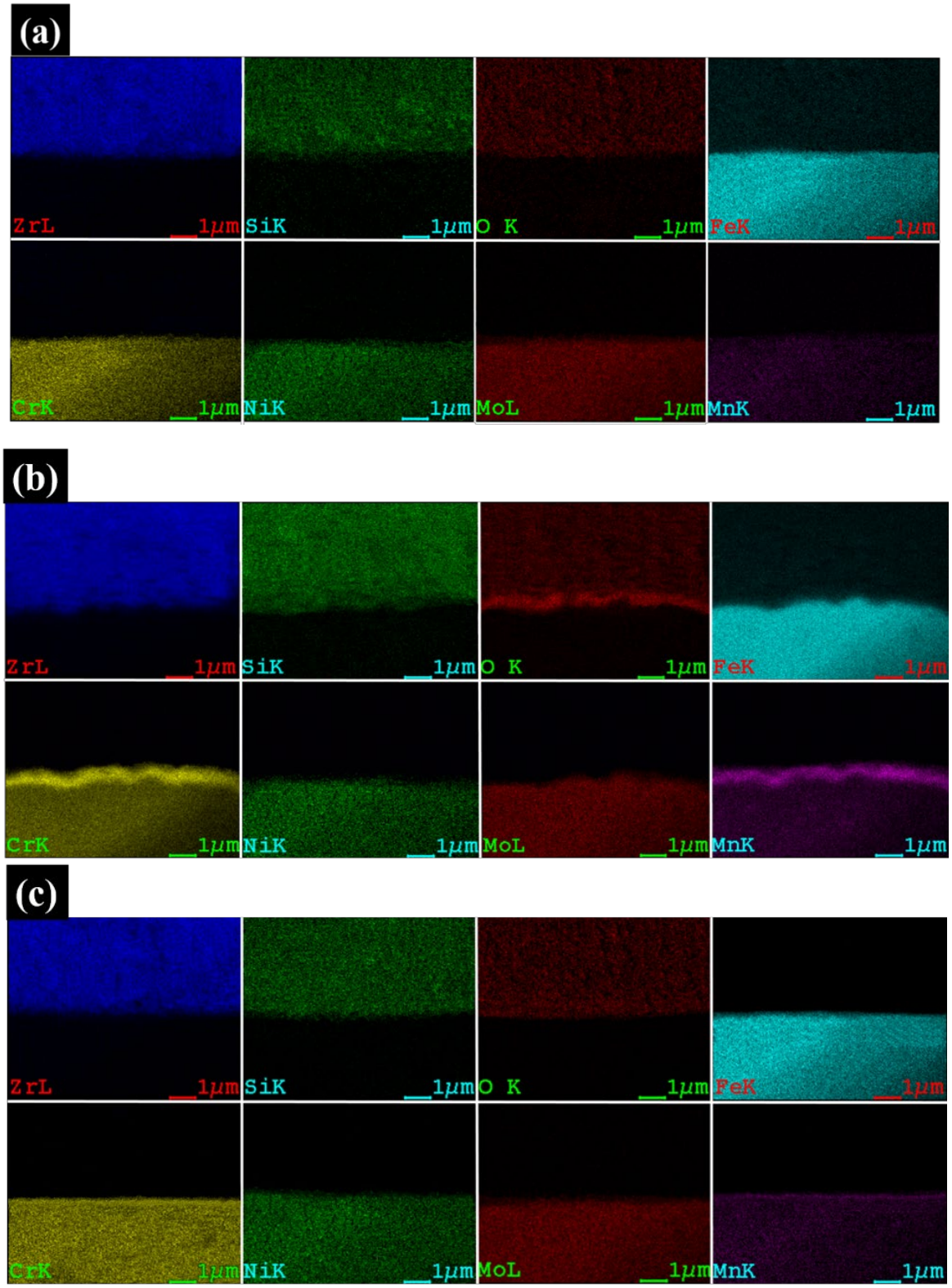

Fig. 15. EDS maps from FIB cross sections of: (a) C_1, (b) C_2, and (c) C_3 coating samples.

3.5 Corrosion behavior of the coatings

Fig. 16 displays the potentiodynamic polarization of the coatings sintered at 1100 °C with their bare substrates after 24 h immersion in an SBF solution at 37 °C. It should be mentioned that the bare substrates were also heat-treated under the same condition at 1100 °C before studying the corrosion behavior. It can be observed that applying the Z10S coating has shifted the polarization curves to a lower current density and more positive potential, indicating that these coatings can successfully protect the stainless steel against corrosion. The polarization parameters including corrosion potential (E_{corr}) and passivation current density (i_p) are extracted from the plots and presented in Table 4. The improvement of passivity behavior could be related to the reduction of the charge transfer by limiting the ion transfer to the substrate owing to the insulating nature of the coatings (i.e., barrier effect).

According to Table 4, the S_2 substrate indicates a more negative E_{corr} value than S_1 and S_3. According to the literature [30], the chemical composition of the anodic oxidized (S_2) and electropolished (S_3) samples is the same; however, the surface of S_2 is porous and rough owing to the presence of an oxide layer with respect to the smooth and homogeneous surface of S_3. This porous surface structure could be the main reason for the degradation observed in the passivation behavior of the S_2 substrate (Fig. 16). Comparing the i_p values of the coatings applied on different substrates, Table 4 indicates that the C_2 coating had the best barrier property. The higher barrier action of the C_2 coating is because of the formation of a dense interlayer as discussed previously.

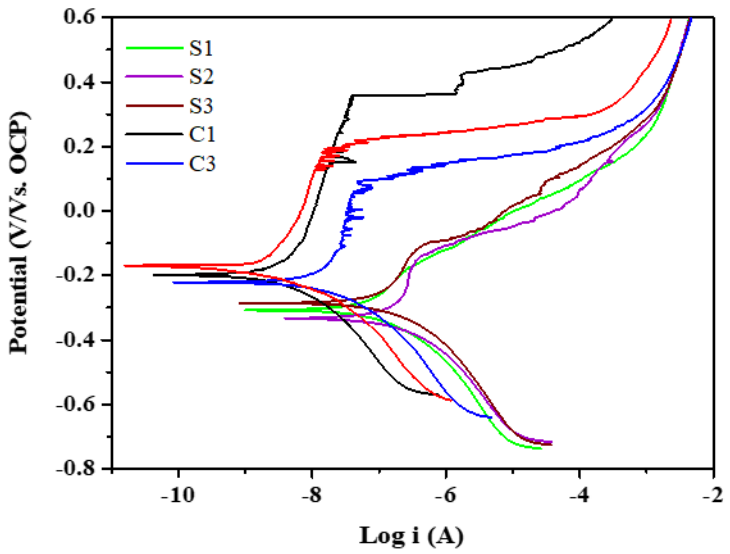

Fig. 16. Potentiodynamic polarization plots drawn after 24 h immersion in SBF solution at 37 °C.

Table 4. Electrochemical parameters extracted from the potentiodynamic polarization plots in Fig. 16

Sample code	E_{corr} (mV/vs. SCE)	i_p (nA cm^{-2})
S_1	-307.01 (3.01)	87.54 (4.23)
S_2	-336.24 (4.03)	100.71 (3.35)
S_3	-288.17 (3.1)	71.63 (5.12)
C_1	-196.15 (7.02)	1.80 (0.2)
C_2	-169.23 (12.24)	0.95 (0.1)
C_3	-221.31 (8.59)	8.97 (0.7)

Similar results were reported by Srinivasan et al. [26]. They applied a ZrO_2-SiO_2 composite on 316L using the sol–gel method and evaluated its corrosion behavior in an SBF solution at 37 °C. The potentiodynamic studies revealed that the passivation current density of the coated sample was reduced by approximately five to ten times compared to the bare substrate. By comparing our results, for example, the C_2 coating, with the above-mentioned research, it can be observed that the reduction of i_p is approximately 105 times with respect to the bare substrate. This

indicates that the ZrO_2-SiO_2 coatings produced using the EPD process in the current study provide higher passivation behavior compared to those prepared through the sol–gel procedure.

To investigate the barrier property of the coatings and verify the results obtained from the polarization tests, EIS measurements were performed and Bode diagrams were drawn as displayed in Fig. 17. The curves related to the substrates (S_1, S_2 and S_3) indicate one time constant (Fig. 17a) representing the passivation behavior of the substrates. In this case, all substrates indicate a hump near 1 Hz. For the S_1 and S_3 samples prepared by mechanical and electropolishing treatments, respectively, the humps are wider and lie in a higher phase angle near 75°. However, the S_2 sample demonstrates a narrower hump at a lower phase angle (approximately 65°) indicating the destructive effect of the anodic oxide layer developed on the 316L stainless steel substrate. As indicated in Fig. 17b, by applying the Z10S composite coating and sintering at 1100 °C, the humps became wider to appear as semi-plateaus and also at higher phase angles with respect to their substrates. For the C_2 coating, the semi-plateau is shifted to approximately 80°, indicating a more effective barrier behavior. Although, the anodic oxidizing treatment had decayed the substrate passivation behavior for the S_2 substrate, the Z10S composite coating deposited on it (i.e., C_2 coating) created the highest barrier property.

An EC model (Fig. 17c) based on a two-layer structure dielectric (an inner compact layer and outer relatively porous layer) was used for fitting the experimental data of the substrates and coatings using the ZVIEW software. This EC consisted of (CPE_{in}-R_{in}) elevated by the barrier role of the oxide film primarily formed on stainless steel substrate, which is enhanced considerably by the presence of Z10S layer, and (CPE_{out}-R_{out}) resulting from the porous outer layer of the passive film, or provided by Z10S coating layer. As indicated, applying the Z10S coating on each substrate did not create an additional time constant. The reason frequently used

for applying the constant phase element (CPE) instead of the ideal capacitor (C) is the presence of porosity, surface roughness, heterogeneity, and probable defects in the coating [53].

According to the electrical elements summarized in Table 5, the R_{in} values were increased significantly by applying the Z10S coating because of the enhanced barrier action provided by the Z10S coating. As indicated, the order of the outer layer resistances was considerably less than that of the inner layer, meaning that the inner layer controls the overall corrosion performance of the coatings. The R_{in} value obtained for C_2 was significantly high (133 MΩ cm^2) compared to the others. The reason must be related to the presence of the interlayer. This interlayer is not formed on the other surfaces.

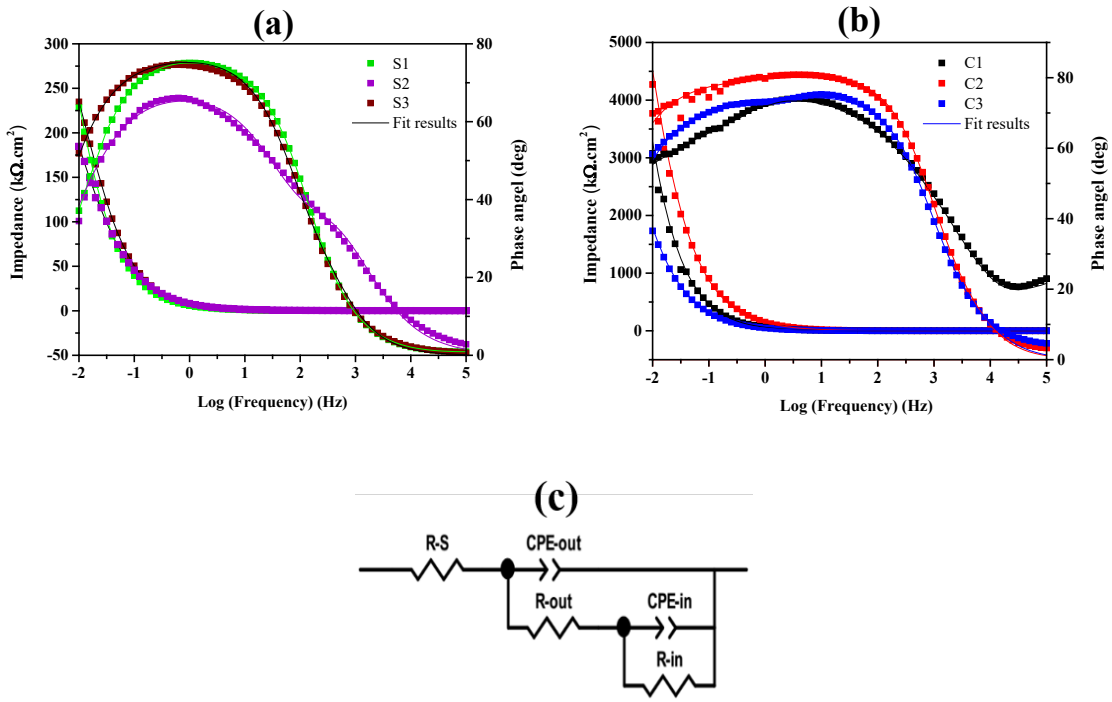

Fig. 17. Bode plots of: (a) substrates, (b) coating samples after 24 h immersion in SBF at 37 °C, and (c) EC model applied for fitting impedance.

Table 5. Electrical elements extracted by fitting EIS data using EC in Fig. 17c

Sample	CPE_{in} ($\mu F.cm^{-2}.s^{n-1}$)	n_{in}	R_{in} ($M\Omega.cm^2$)	CPE_{out} ($\mu F.cm^{-2}.s^{n-1}$)	n_{out}	R_{out} ($\Omega.cm^2$)
S_1	17.34 (4.7)	0.84 (0.01)	0.41 (0.01)	19.85 (0.02)	0.86 (0.01)	104.31(5.64)
S_2	34.7 (4.5)	0.72 (0.01)	0.36 (0.01)	27.28 (0.03)	0.74 (0.02)	84.9 (7.10)
S_3	9.6 (2.3)	0.87 (0.02)	0.53 (0.01)	14.9 (1.20)	0.93 (0.02)	121.1 (5.25)
C_1	0.234 (0.01)	0.81 (0.01)	10.91 (2.3)	2.97 (0.01)	0.86 (0.01)	271.5 (8.65)
C_2	0.103 (0.01)	0.73 (0.03)	133.00 (12.18)	0.59 (0.05)	0.81 (0.03)	657 (19.76)
C_3	0.387 (0.02)	0.83 (0.01)	6.3 (0.31)	7.77 (0.02)	0.97 (0.04)	130.5 (3.14)

3.6. 3D tomography and mechanism of dense interlayer formation at the interface

Because the C_2 sample demonstrated the best corrosion performance owing to the formation of a dense oxide interlayer after the sintering process, we studied its interface structure using a 3D FIB-tomography technique. Tomography was performed using a dual-beam FIB system. In this method, the stage was tilted to 52° until the sample surface was located normal to the ion beam source. A trench with sufficient space and depth around the region of interest (ROI) was milled using an ion beam source. The prepared ROI was sliced and the obtained SEM images from each slice were used to create a 3D reconstruction. Fig. 18 illustrates the SEM image of the ROI after milling by the Ga ion beam source with a current density of 21 nA.

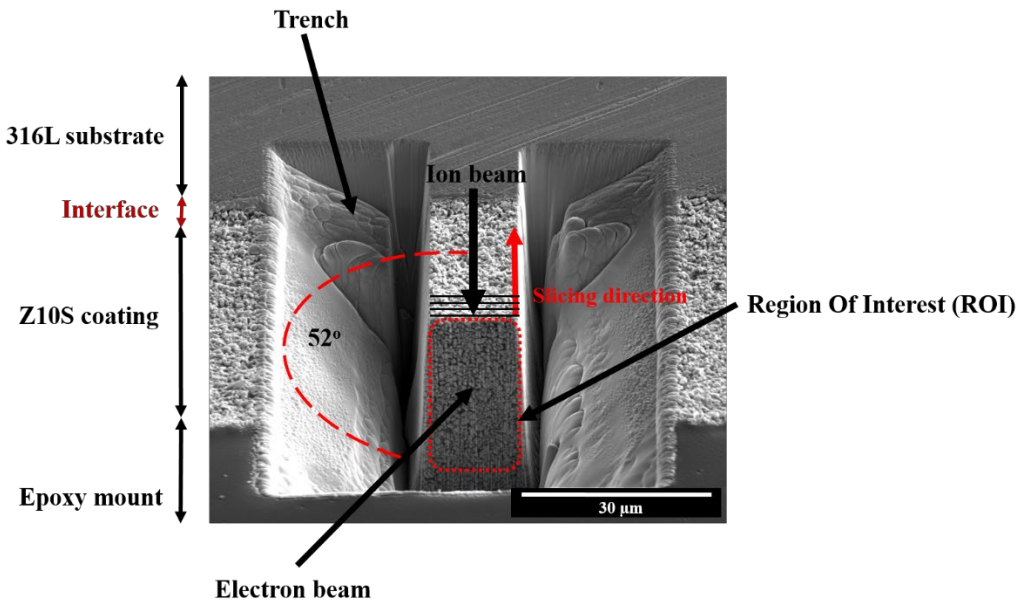

Fig. 18. SEM image from region of interest for 3D reconstruction using slice and view method.

The 3D tomography from the interface of the C_2 sample is represented in Fig. 19. As indicated, the interface illustrates a dual layer structure consisting of an inner porous layer contacting the stainless steel substrate and a top outer dense layer. The inner porous layer is the anodic oxide layer formed earlier by the anodic oxidizing treatment of the substrate surface, whereas the outer dense layer is formed by the Z10S particles entering into the pores of the anodic oxide layer following the integration. As discussed previously, during the sintering process, the anodic oxide layer rich in chromium and manganese elements can integrate with the Z10S particles embedded earlier in the porosity of this oxide layer, which develops a dense interlayer. This layer is responsible for the strong chemical bonding of the Z10S coating to the substrate enhancing the coating adhesion. Conversely, this dense layer acts as a promising barrier against the diffusion of corrosive agents. However, because the chemical composition of the 316L substrate is different from the anodic oxidized layer, it leads to the creation of a mismatch in their thermal expansion

coefficients. In this manner, defects (detachments) inevitably develop at the interface of the interlayer/base metal during the sintering process.

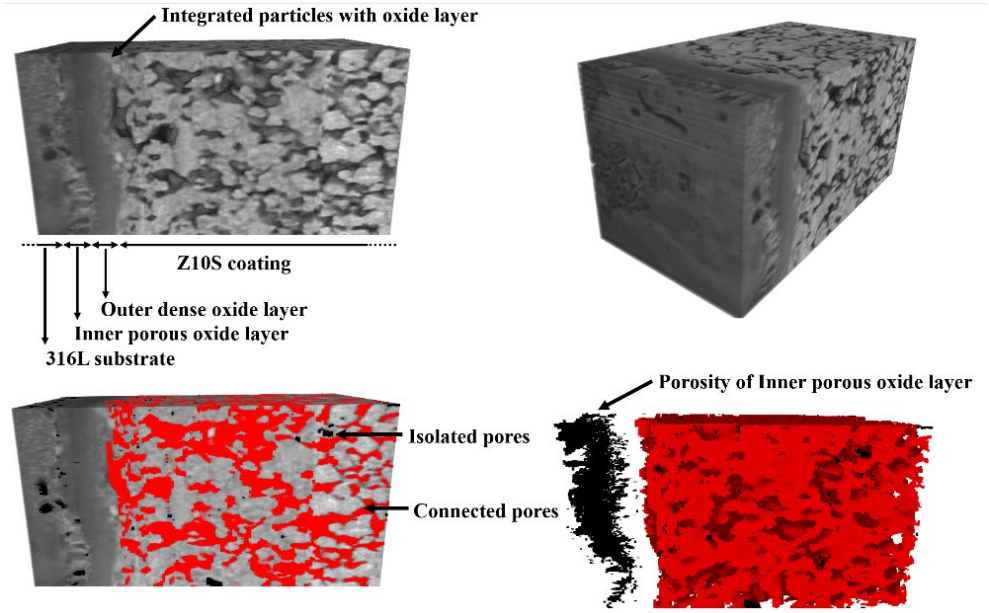

Fig. 19. 3D visualization from interface of C_2 sample after sintering (different views).

To study the porosity and packing density of the layers across the interface, one slice of each layer was cut from the 3D image as displayed in Fig. 20. The slice related to the coating (Fig. 20a) indicates that the Z10S particles are attached firmly together after the sintering process. The coating is composed of connected pores as represented by the 3D pore reconstructed images provided in Fig. 19. Figs. 20b and c clearly indicate the slices from dense and porous layers at the coating/substrate interface, respectively. (The structure of the coating and interface can be overviewed by a short video prepared from the serial sectioning of the slice moving in the z direction through the coating as presented in the supplementary information section). According to the results obtained from the 3D visualization analysis, we proposed a model for the interlayer formation. Fig. 21 displays a schematic describing the stepwise formation mechanism of the interlayer and the Z10S coating on the anodic oxidized surface of the 316L substrate.

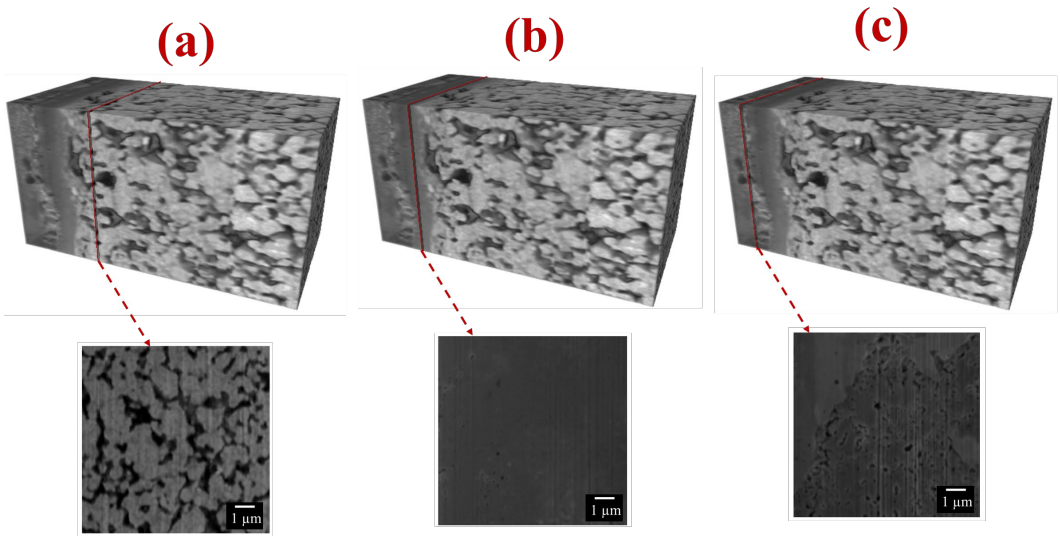

Fig. 20. SEM images of slices selected from: (a) coating layer and interlayer including, (b) dense layer, and (c) porous layer.

Fig. 21a represents the porous oxide layer formed on the surface of the 316L substrate after anodic oxidation treatment. This porous structure was also detected through the IFM image displayed in Fig. 6b. The Ra parameter for the anodic oxidized substrate (Table 2) obtained was approximately 1.46 µm, which is similar to the thickness of the dense layer (approximately 1.30 µm) supported by the FIB-cross section image in Fig. 14c. Nanoporous oxide film with 3.2 µm thickness was reported on stainless steel by Asoh et al. [54]. They suggested that this nanoporous oxide film could act as a highly suitable host to encourage HA formation in an SBF, which is attributable to the empty pore volume of the layer [54]. Similarly, from Fig. 21b, Z10S particles are deposited on the porous surface of the 316L substrate to form a homogeneous layer. Particles having smaller size than the pore diameters can enter into the pores; however, the pores can be blocked with the larger particles leaving significant empty spaces inside the pores. In this manner, the trapped particles have not been sufficiently compacted to form a dense structure during sintering, resulting in a porous layer at the bottom of the pores (Fig. 21c). The dense layer

is also formed by the integration of the Z10S particles with the anodic oxide layer at the upper parts of the surface porosities as indicated in Fig. 21c. Further, detachments can be observed at the interface of the oxide layer and steel substrate raised by their different thermal expansion coefficients (Fig. 21c).

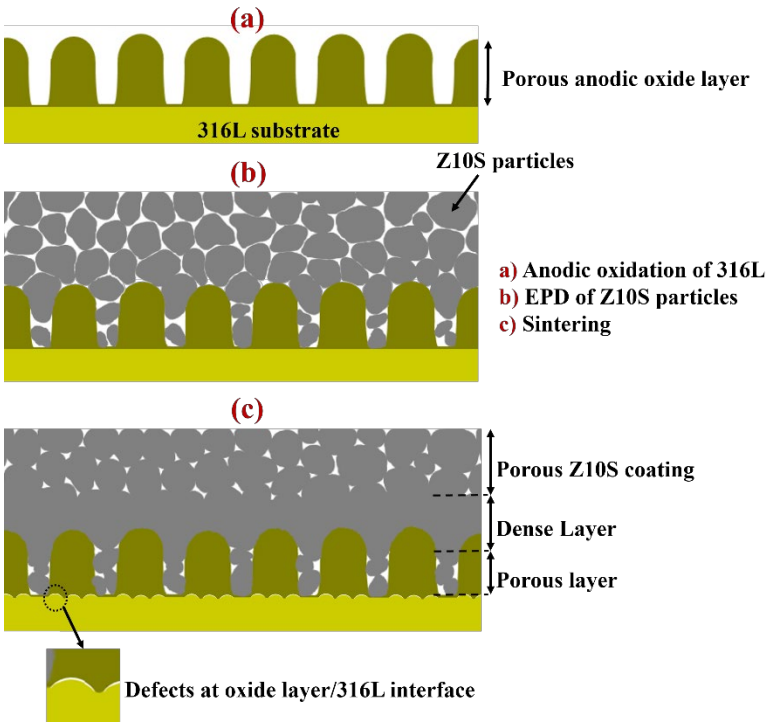

Fig. 21. Schematic representation of proposed model of formation of Z10S coating on anodic oxidized 316L.

4. Conclusions

A stable suspension of synthesized ZrO_2-10 mol.% SiO_2 nanocomposite particles in EtOH was made through modification using 3 wt.% polyethyleneimine as a surfactant and adding 0.3 g/L iodine as a charging agent. A nanocomposite coating consisting of monoclinic ZrO_2 and amorphous SiO_2 was obtained using a cathodic EPD process. Three surface treatments including mechanical polishing, electropolishing, and anodic oxidizing were applied to prepare the surface

of a 316L substrate before the EPD process. The following conclusions are supported by the obtained results:

1- The sintered coated samples revealed high inner layer resistances because of the presence of the ZrO_2-SiO_2 layer, which enhanced the barrier effect of the passive oxide films formed primarily on the stainless steel substrate. The inner layer determined the overall corrosion performance of the coatings.

2- For the coating produced by the EPD process on the anodic oxidized substrate, sintering at 1100 ˚C created a dense interlayer through the integration of ZrO_2-SiO_2 composite particles embedded earlier inside the porosity of the anodic oxide layer. This dense interlayer revealed a high inner layer resistance of 133 MΩ cm^{-2}, which is at least 13 times greater than those from other samples. In this manner, this coating demonstrated the lowest passivation current density of 0.95 nA cm^{-2} after 24 h immersion in an SBF solution at 37 °C.

3- Based on the 3D FIB tomography results from the interface of the ZrO_2-SiO_2 coating applied on the anodic oxidized treated substrate, it was a dual layer structure including an inner porous layer and outer dense layer. The pores of the anodic oxide layer were partially filled by Z10S particles leading to the formation of the inner porous layer at the bottom of the pores. Conversely, the dense layer was formed by the integration of Z10S particles with the anodic oxide layer at the upper parts of the surface porosities.

4- Owing to the difference between the thermal expansion coefficients of the 316L substrate and Z10S coating, detachments were developed at the interface of the coating and steel substrate during the sintering process for all cases.

Acknowledgment

The authors would like to acknowledge the financial support by the Research Council of Norway through the HyF-Lex (244068/E30) project. The Research Council of Norway is acknowledged for support to NTNU NanoLab through the Norwegian Micro- and Nano-Fabrication Facility, Norfab (197411/V30).

References

[1] S. Radice, P. Kern, G. Bürki, J. Michler, M. Textor, Electrophoretic deposition of zirconia-Bioglass® composite coatings for biomedical implants, Journal of Biomedical Materials Research Part A, 82A (2007) 436-444.
[2] A. Parsapour, S.N. Khorasani, M.H. Fathi, Effect of Surface Treatment and Metallic Coating on Corrosion Behavior and Biocompatibility of Surgical 316L Stainless Steel Implant, Journal of Materials Science & Technology, 28 (2012) 125-131.
[3] M. Jokar, S. Darvishi, R. Torkaman, M. Kharaziha, M. Karbasi, Corrosion and bioactivity evaluation of nanocomposite PCL-forsterite coating applied on 316L stainless steel, Surface and Coatings Technology, 307 (2016) 324-331.
[4] S.K. Yen, M.J. Guo, H.Z. Zan, Characterization of electrolytic ZrO_2 coating on Co–Cr–Mo implant alloys of hip prosthesis, Biomaterials, 22 (2001) 125-133.
[5] T. Hryniewicz, R. Rokicki, K. Rokosz, Surface characterization of AISI 316L biomaterials obtained by electropolishing in a magnetic field, Surface and Coatings Technology, 202 (2008) 1668-1673.
[6] S. Tiwari, T. Mishra, M. Gunjan, A. Bhattacharyya, T. Singh, R. Singh, Development and characterization of sol–gel silica–alumina composite coatings on AISI 316L for implant applications, Surface and Coatings Technology, 201 (2007) 7582-7588.
[7] D.A. Armitage, T.L. Parker, D.M. Grant, Biocompatibility and hemocompatibility of surface-modified NiTi alloys, Journal of Biomedical Materials Research Part A, 66A (2003) 129-137.
[8] M. Fathi, A. Doostmohammadi, Bioactive glass nanopowder and bioglass coating for biocompatibility improvement of metallic implant, Journal of materials processing technology, 209 (2009) 1385-1391.
[9] C.-Y. Chiu, H.-C. Hsu, W.-H. Tuan, Effect of zirconia addition on the microstructural evolution of porous hydroxyapatite, Ceramics International, 33 (2007) 715-718.
[10] C. Piconi, A.A. Porporati, Bioinert ceramics: Zirconia and alumina, in: Handbook of Bioceramics and Biocomposites, Springer, 2016, pp. 59-89.
[11] G. Wang, F. Meng, C. Ding, P.K. Chu, X. Liu, Microstructure, bioactivity and osteoblast behavior of monoclinic zirconia coating with nanostructured surface, Acta Biomaterialia, 6 (2010) 990-1000.
[12] X. Liu, A. Huang, C. Ding, P.K. Chu, Bioactivity and cytocompatibility of zirconia (ZrO_2) films fabricated by cathodic arc deposition, Biomaterials, 27 (2006) 3904-3911.
[13] F. del Monte, W. Larsen, J.D. Mackenzie, Stabilization of tetragonal ZrO_2 in ZrO_2–SiO_2 binary oxides, Journal of the American Ceramic Society, 83 (2000) 628-634.
[14] L.L. Hench, The story of Bioglass®, Journal of Materials Science: Materials in Medicine, 17 (2006) 967-978.
[15] S.-H. Rhee, J.-Y. Choi, H.-M. Kim, Preparation of a bioactive and degradable poly (ε-caprolactone)/silica hybrid through a sol–gel method, Biomaterials, 23 (2002) 4915-4921.

[16] N. Hijón, M.V. Cabanas, J. Pena, M. Vallet-Regí, Dip coated silicon-substituted hydroxyapatite films, Acta biomaterialia, 2 (2006) 567-574.
[17] M. Crisan, M. Gartner, L. Predoana, R. Scurtu, M. Zaharescu, R. Gavrila, Sol–Gel SiO_2-ZrO_2 Coatings for Optical Applications, Journal of sol-gel science and technology, 32 (2004) 167-172.
[18] M. Morks, A. Kobayashi, Development of ZrO_2/SiO_2 bioinert ceramic coatings for biomedical application, Journal of the mechanical behavior of biomedical materials, 1 (2008) 165-171.
[19] O. Unal, T.E. Mitchell, A.H. Heuer, Microstructures of Y_2O_3-Stabilized ZrO_2 Electron Beam-Physical Vapor Deposition Coatings on Ni-Base Superalloys, Journal of the American Ceramic Society, 77 (1994) 984-992.
[20] M.K. Baek, S.J. Park, D.J. Choi, Synthesis of zirconia (ZrO_2) nanowires via chemical vapor deposition, Journal of Crystal Growth, 459 (2017) 198-202.
[21] A. Śmieszek, A. Donesz-Sikorska, J. Grzesiak, J. Krzak, K. Marycz, Biological effects of sol–gel derived ZrO_2 and SiO_2/ZrO_2 coatings on stainless steel surface—In vitro model using mesenchymal stem cells, Journal of biomaterials applications, 29 (2014) 699-714.
[22] L. Besra, M. Liu, A review on fundamentals and applications of electrophoretic deposition (EPD), Progress in materials science, 52 (2007) 1-61.
[23] A.R. Boccaccini, J.H. Dickerson, Electrophoretic deposition: fundamentals and applications, in, ACS Publications, 2013.
[24] M.A. Villegas, Chemical and microstructural characterization of sol–gel coatings in the ZrO_2–SiO_2 system, Thin Solid Films, 382 (2001) 124-132.
[25] F.L. Perdomo, P. De Lima-Neto, M.A. Aegerter, L.A. Avaca, Sol-Gel Deposition of ZrO_2 Films in Air and in Oxygen-Free Atmospheres for Chemical Protection of 304 Stainless Steel: A Comparative Corrosion Study, Journal of Sol-Gel Science and Technology, 15 (1999) 87-91.
[26] A. Srinivasan, N. Rajendran, Electrochemical Corrosion and In Vitro Bioactivity of SiO_2:ZrO_2-Coated 316L Stainless Steel in Simulated Body Fluid, Journal of Materials Engineering and Performance, 24 (2015) 3056-3067.
[27] K. Pardun, L. Treccani, E. Volkmann, P. Streckbein, C. Heiss, G.L. Destri, G. Marletta, K. Rezwan, Mixed zirconia calcium phosphate coatings for dental implants: Tailoring coating stability and bioactivity potential, Materials Science and Engineering: C, 48 (2015) 337-346.
[28] M. Morks, Fabrication and characterization of plasma-sprayed HA/SiO_2 coatings for biomedical application, Journal of the mechanical behavior of biomedical materials, 1 (2008) 105-111.
[29] S. Radice, P. Kern, G. Bürki, J. Michler, M. Textor, Electrophoretic deposition of zirconia-Bioglass® composite coatings for biomedical implants, Journal of Biomedical Materials Research Part A: An Official Journal of The Society for Biomaterials, The Japanese Society for Biomaterials, and The Australian Society for Biomaterials and the Korean Society for Biomaterials, 82 (2007) 436-444.
[30] S. Habibzadeh, L. Li, D. Shum-Tim, E.C. Davis, S. Omanovic, Electrochemical polishing as a 316L stainless steel surface treatment method: Towards the improvement of biocompatibility, Corrosion Science, 87 (2014) 89-100.
[31] P. Sarkar, P.S. Nicholson, Electrophoretic deposition (EPD): mechanisms, kinetics, and application to ceramics, Journal of the American Ceramic Society, 79 (1996) 1987-2002.
[32] J.H. Dickerson, A.R. Boccaccini, Electrophoretic deposition of nanomaterials, Springer, 2011.
[33] K. Moritz, E. Müller, Investigation of the electrophoretic deposition behaviour of non-aqueous ceramic suspensions, Journal of materials science, 41 (2006) 8047-8058.
[34] K. Maca, H. Hadraba, J. Cihlar, Electrophoretic deposition of alumina and zirconia: I. Single-component systems, Ceramics international, 30 (2004) 843-851.
[35] C. Herring, Effect of change of scale on sintering phenomena, Journal of Applied Physics, 21 (1950) 301-303.
[36] P. Mondragon-Cortez, G. Vargas-Gutierrez, Electrophoretic deposition of hydroxyapatite submicron particles at high voltages, Materials Letters, 58 (2004) 1336-1339.
[37] T.F. Tadros, Dispersion of Powders: in Liquids and Stabilization of Suspensions, John Wiley & Sons, 2012.

[38] T.F. Tadros, Dispersion of powders in liquids and stabilization of suspensions, John Wiley & Sons, 2012.
[39] J. Wang, L. Gao, Adsorption of polyethylenimine on nanosized zirconia particles in aqueous suspensions, Journal of colloid and interface science, 216 (1999) 436-439.
[40] D. Liu, C. Perry, R. Ingel, Infrared spectra in nonstoichiometric yttria-stabilized zirconia mixed crystals at elevated temperatures, Journal of applied physics, 64 (1988) 1413-1417.
[41] G. Monros, M. Marti, J. Carda, M. Tena, P. Escribano, M. Anglada, Effect of hydrolysis time and type of catalyst on the stability of tetragonal zirconia-silica composites synthesized from alkoxides, Journal of materials science, 28 (1993) 5852-5862.
[42] F. Monte, W. Larsen, J.D. Mackenzie, Stabilization of Tetragonal ZrO_2 in ZrO_2–SiO_2 Binary Oxides, Journal of the American Ceramic Society, 83 (2000) 628-634.
[43] Y. Wang, D. Wu, Q. Wei, D. Wei, T. Yan, L. Yan, L. Hu, B. Du, Rapid removal of Pb(II) from aqueous solution using branched polyethylenimine enhanced magnetic carboxymethyl chitosan optimized with response surface methodology, Scientific Reports, 7 (2017) 10264.
[44] F. Chen, M. Liu, Preparation of yttria-stabilized zirconia (YSZ) films on La0. 85Sr0. 15MnO_3 (LSM) and LSM–YSZ substrates using an electrophoretic deposition (EPD) process, Journal of the European Ceramic Society, 21 (2001) 127-134.
[45] H. Hamaker, Formation of a deposit by electrophoresis, Transactions of the Faraday Society, 35 (1940) 279-287.
[46] H.C. Hamaker, Formation of a deposit by electrophoresis, Transactions of the Faraday Society, 35 (1940) 279-287.
[47] R.E. Loehman, Characterization of ceramics, Momentum Press, 2010.
[48] H. Hadraba, J. Klimes, K. Maca, Crack propagation in layered Al_2O_3/ZrO_2 composites prepared by electrophoretic deposition, Journal of materials science, 42 (2007) 6404-6411.
[49] I.M. Low, 1 - Advances in ceramic matrix composites: an introduction, in: I.M. Low (Ed.) Advances in Ceramic Matrix Composites, Woodhead Publishing, 2014, pp. 1-6.
[50] F. Del Monte, W. Larsen, J.D. Mackenzie, Chemical Interactions Promoting the ZrO_2 Tetragonal Stabilization in ZrO_2–SiO_2 Binary Oxides, Journal of the American Ceramic Society, 83 (2000) 1506-1512.
[51] K. Kamada, M. Tokutomi, N. Enomoto, J. Hojo, Incorporation of oxide nanoparticles into barrier-type alumina film via anodic oxidation combined with electrophoretic deposition, Journal of Materials Chemistry, 15 (2005) 3388-3394.
[52] X. Nie, A. Leyland, A. Matthews, Deposition of layered bioceramic hydroxyapatite/TiO_2 coatings on titanium alloys using a hybrid technique of micro-arc oxidation and electrophoresis, Surface and Coatings Technology, 125 (2000) 407-414.
[53] N. Karimi, M. Kharaziha, K. Raeissi, Electrophoretic deposition of chitosan reinforced graphene oxide-hydroxyapatite on the anodized titanium to improve biological and electrochemical characteristics, Materials Science and Engineering: C, 98 (2019) 140-152.
[54] H. Asoh, M. Nakatani, S. Ono, Fabrication of thick nanoporous oxide films on stainless steel via DC anodization and subsequent biofunctionalization, Surface and Coatings Technology, 307 (2016) 441-451.